RSC Advances

PAPER

View Article Online
View Journal | View Issue

Cite this: *RSC Adv.*, 2023, **13**, 23236

Molecular dynamics exploration of helium bubble nucleation and growth mechanisms in $Fe_{70}Ni_{11}Cr_{19}$ austenitic stainless steel

X. W. Zhou *

The growth of helium bubbles impacts structural integrity of materials in nuclear applications. Understanding helium bubble nucleation and growth mechanisms is critical for improved material applications and aging predictions. Systematic molecular dynamics simulations have been performed to study helium bubble nucleation and growth mechanisms in $Fe_{70}Ni_{11}Cr_{19}$ stainless steels. First, helium cluster diffusivities are calculated at a variety of helium cluster sizes and temperatures for systems with and without dislocations. Second, the process of diffusion of helium atoms to join existing helium bubbles is not deterministic and is hence studied using ensemble simulations for systems with and without vacancies, interstitials, and dislocations. We find that bubble nucleation depends on diffusion of not only single helium atoms, but also small helium clusters. Defects such as vacancies and dislocations can significantly impact the diffusion kinetics due to the trapping effects. Vacancies always increase the time for helium atoms to join existing bubbles due to the short-range trapping effect. This promotes bubble nucleation as opposed to bubble growth. Interestingly, dislocations can create a long-range trapping effect that reduces the time for helium atoms to join existing bubbles. This can promote bubble growth within a certain region near dislocations.

Received 13th June 2023
Accepted 27th July 2023

DOI: 10.1039/d3ra03969b

rsc.li/rsc-advances

1. Introduction

Due to either energetic particle irradiation or radioactive decay,[1,2] structural alloys used in nuclear applications often collect helium (He) content over time. As He atoms do not bond with metals, they separate out to form internal bubbles. These He bubbles significantly embrittle the materials,[3–9] and are often the determining factor for structural failures. Extensive experimental[1–6,8,10–15] and modeling[16–24] studies have been performed to understand the He effects. These studies indicate that the lifetimes of materials critically depend on the number, size, and spatial populations of He bubbles. For instance, a high density of bubbles at grain boundaries is believed to be more detrimental than if they are in the bulk.[1,4–6,8,11–16] The number, size, and spatial populations of He bubbles are determined by how bubbles nucleate and grow. Improved material applications and aging predictions, therefore, require a fundamental understanding of He bubble nucleation and growth mechanisms. These mechanisms, however, cannot be easily obtained from experiments.

As a relevant example, $Fe_{70}Ni_{11}Cr_{19}$ face centered cubic (FCC) alloys (close to 300-series stainless steels) have been used as structural materials for nuclear applications.[25,26] Upon reaching an equilibrium with a possible ^3H gas environments, the materials contain an internal ^3H concentration that is elevated near defects especially dislocations.[27] Due to the $^3H \rightarrow He$ decay, He interstitial atoms are continuously born at the ^3H locations. These He atoms diffuse rapidly[28] so they can quickly find each other to form He clusters. Unlike the near repulsive He interactions in the pure He gas phase, He clusters in metals are strongly attractive.[28] Hence, He clusters will no longer dissociate. The traditional *self-trapping theory* of bubble nucleation[29–31] assumes that He clusters of any size (containing 2 or more He atoms) are immobile. This means that whenever two He interstitial atoms meet and form a dimer, it essentially nucleates a bubble because the He atoms become trapped in their current location, eventually evolving to a bubble when more He atoms arrive. As an alternative bubble nucleation mechanism, the *defect-trapping theory* assumes that He are trapped at defects[32–35] such as vacancies, self-interstitial atoms (SIAs), impurity/alloy solutes, dislocations, and grain boundaries. The *defect-trapping mechanism* has important implications as it suggests that defects can be utilized to control He bubble number, size, and spatial populations.

Density-functional-theory (DFT) and molecular dynamics (MD) studies[35–39] indicate that He dimer clusters are still mobile. It is reasonable to assume that He clusters only become immobile when they are large enough to displace metal atoms resulting in metal vacancies that trap He atoms. Hence, a study

Sandia National Laboratories, Livermore, California 94550, USA. E-mail: xzhou@sandia.gov

of He bubble nucleation mechanisms is essentially a study of He cluster diffusion for all cluster sizes below a critical size where clusters are mobile.

Once a significantly big bubble is developed, a considerable number of metal atoms are displaced into other places. This results in the formation of various defects such as interstitials, vacancies, and dislocations. The bubble also creates stress field in surrounding areas. Defects and stress fields both impact the subsequent He cluster diffusion and He arrival rates at existing bubbles. Hence, a study of He bubble growth mechanisms must involve a study of time distribution for He atoms to join existing bubbles in the presence of defects and bubble stress fields.

The objectives of the present work are to perform extensive MD simulations on $Fe_{70}Ni_{11}Cr_{19}$ to understand (1) He cluster diffusivities at different cluster sizes with and without dislocations, and (b) time distributions of an He atom to join an existing bubble with a given pressure, considering samples without defects, and with vacancies, interstitials, and dislocations.

2. Methods

All simulations are performed using the parallel MD code LAMMPS.[40–42] A time step size of 0.0005 ps is used. All temperature and pressure controls are achieved *via* integration on Nose–Hoover style non-Hamiltonian equations of motion with time constants of 0.05 ps and 0.5 ps for thermostat and barostat respectively. The Fe–Ni–Cr–H–He embedded-atom method potential[28,43] is used to define interatomic forces. This potential incorporates the interactions between He and electrons as revealed from density-functional theory calculations, and therefore correctly captures the paradoxical behavior that He–He interactions are repulsive in the gas phase but are strongly attractive in metals.[28] Simulation details for cluster diffusivities and He-to-bubble time statistics are described separately in the following, but a brief summary of scales of simulations is given in the Appendix.

2.1 Cluster diffusivities

Cluster diffusivities are calculated following the previous MD approach that statistically account for all jump paths encountered during diffusion.[44–49] Briefly, He cluster sizes between 1 and 10 are considered. For each cluster size, MD simulations are performed at 13 temperatures (300 K, 325 K, 350 K, …, 600 K). After an initial 0.2 ns for equilibration, the mean square displacement of the He cluster is tracked for the following 70 ns. Note that the 0.2 ns is sufficient because it is intended to equilibrate the population of atom velocities which can be achieved through a few atomic vibrations. The linear portion of the mean square displacement as a function of time is used to fit a diffusivity D based on eqn (1),[44]

$$\overline{R^2} = 6Dt \quad (1)$$

where $\overline{R^2}$, D, and t represent mean square displacement, diffusivity, and time respectively. To ensure that only linear portion is fitted, the entire mean square displacement *vs.* time curve is first visualized and the range of fit is determined from the visualization. The diffusivities thus obtained at different temperatures are then fitted to the Arrhenius equation to derive both pre-exponential factor D_0 and diffusion energy barrier Q:

$$D = D_0 \exp\left(-\frac{Q}{k_B T}\right) \quad (2)$$

where k_B and T are Boltzmann constant and temperature respectively. All simulations are performed using a zero-pressure NPT ensemble to relax system volume.

$Fe_{70}Ni_{11}Cr_{19}$ alloys with and without edge dislocations are studied under periodic boundary conditions in all three directions. Orientations of systems are illustrated in Fig. 1. For the

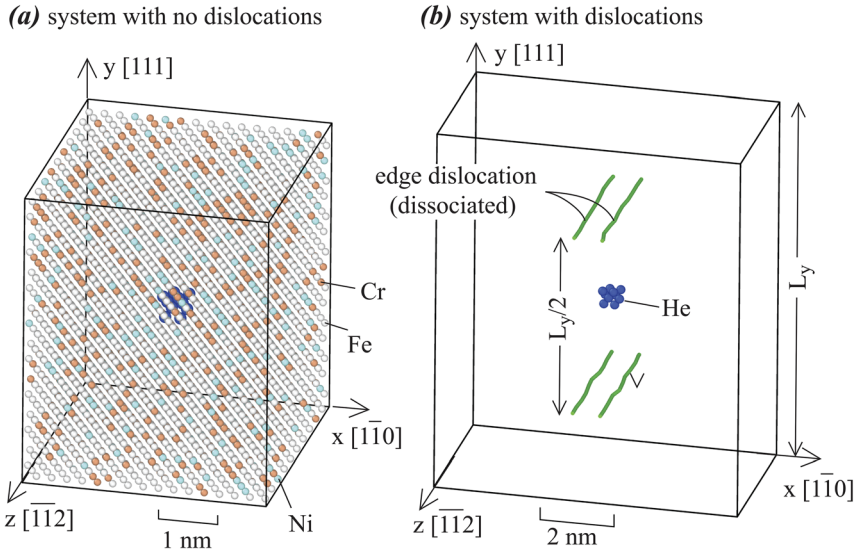

Fig. 1 Crystal geometries used for He cluster diffusion simulations: (a) systems without dislocations (white balls: Fe, blue balls: Ni, orange balls: Cr), and (b) systems with dislocations.

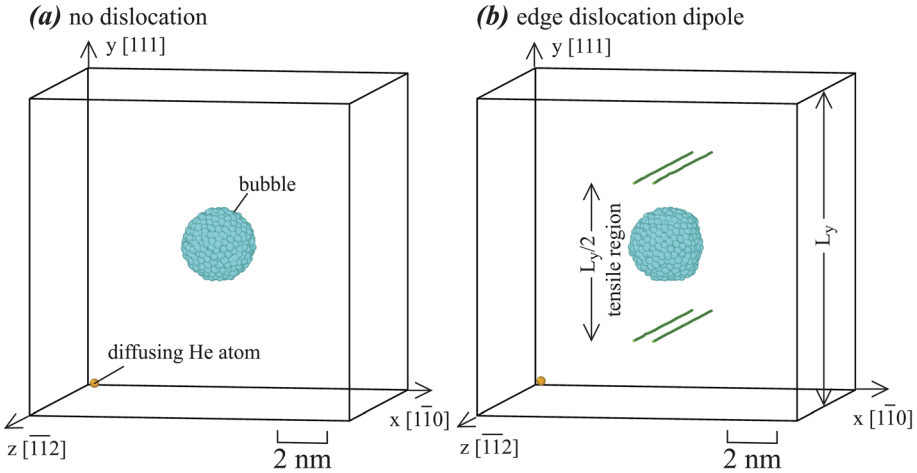

Fig. 2 Crystal geometries used for He-to-bubble simulations: (a) systems without dislocations, and (b) systems with dislocations.

dislocation-free case shown in Fig. 1(a), the system contains ~41 Å in x, ~50 Å in y, and ~44 Å in z, with 7680 metal atoms. For the dislocation-containing case shown in Fig. 1(b), the system contains ~82 Å in x, ~100 Å in y, and ~44 Å in z, with 30 240 metal atoms. A larger x–y dimension is needed for the dislocation case to minimize dislocation interactions and retain a proper dislocation stress field. To enable the periodic boundary conditions, we study dislocation dipoles and the dipole distance is half of the y dimension so that all dislocations are equally spaced. Dislocation lines are along the z axis, with an edge Burgers vector $\mathbf{b} = [1\bar{1}0]/2$. Such dislocations can be easily created.[50,51] During simulations, the perfect edge dislocations are naturally dissociated into a pair of Shockley partial dislocations.

2.2 He-to-bubble time statistics

Orientations of the $Fe_{70}Ni_{11}Cr_{19}$ alloys used for calculating the He-to-bubble time statistics are shown in Fig. 2. In Fig. 2(a), the system contains ~128 Å in x, ~126 Å in y, and ~133 Å in z, with 180 000 metal atoms. In the center of the system, 1452 metal atoms are replaced by 1428 He atoms to create a He bubble. Using time-averaged MD calculations of atomic stresses and atomic Voronoi volumes[40–42] over a 0.1 ns period at 800 K, He bubble pressure is calculated as

$$P = -\frac{\sum_i \left(\sigma_{i,xx} + \sigma_{i,yy} + \sigma_{i,zz}\right)}{3\sum_i \Omega_i} \quad (3)$$

where $\sigma_{i,xx}$, $\sigma_{i,yy}$, $\sigma_{i,zz}$ are time-averaged normal stresses on atom i, and Ω_i is time-averaged Voronoi volume of atom i, and the summation is over all the He atoms in the bubble. Note that the right hand side of eqn (3) needs to be divided by volume because the "stress" calculated from LAMMPS is actually a "stress·volume" quantity. Counterintuitively, the time-averaged calculations produce much more converged results than energy minimization simulations.[50–52] As a result, we perform the simulations twice using different random number seeds and get an identical bubble pressure of 6.6 GPa.

A diffusing He atom is created at the corner far away from the bubble. MD simulations are then performed at 800 K for a total period of 5 ns using a zero-pressure NPT ensemble under periodic boundary conditions in all three directions. Once the diffusing He is found to join the bubble, the time is recorded. A thousand such simulations are conducted to construct a time distribution.

Fig. 2(a) does not have dislocations. To explore effects of dislocations, an edge dislocation dipole is inserted into the system with the same orientations and dimensions. The dislocation lines are along z with an edge Burgers vector $\mathbf{b} = [1\bar{1}0]/2$, which are naturally dissociated into Shockley partials during simulations. Again, we perform a thousand simulations to construct time distribution. We also perform two additional sets of thousand simulations with 0.2% vacancies and 0.2% interstitials respectively to construct the corresponding time distributions. Based on random numbers generated, vacancies are introduced by randomly removing metal atoms, and interstitials are introduced by randomly adding metal atoms into octahedral interstitial sites, until they match the corresponding composition ratios.

3. Results and discussions

3.1 Cluster diffusivities

Diffusivities D are calculated from 260 MD simulations at 10 He cluster sizes (from He_1 to He_{10}) and 13 temperatures (from 300 K to 600 K) with and without dislocations. The results of these diffusivities are summarized in Fig. 3(a) for systems with no dislocations and Fig. 3(b) for systems with dislocations, where lines are fits to eqn (2). Note that in Fig. 3, $\ln(D) < -20$ means that D is essentially ~0 so that $\ln(D)$ is ill-defined and is simply placed at the −20 line. Fig. 3 only shows results for cluster sizes between 1 and 7. Cluster sizes above 7 are not included because diffusivities are extremely low.

Fig. 3(a) indicates that for the dislocation-free cases, $\ln(D)$ is linear with $(k_B T)^{-1}$ for He cluster sizes between 1 and 5.

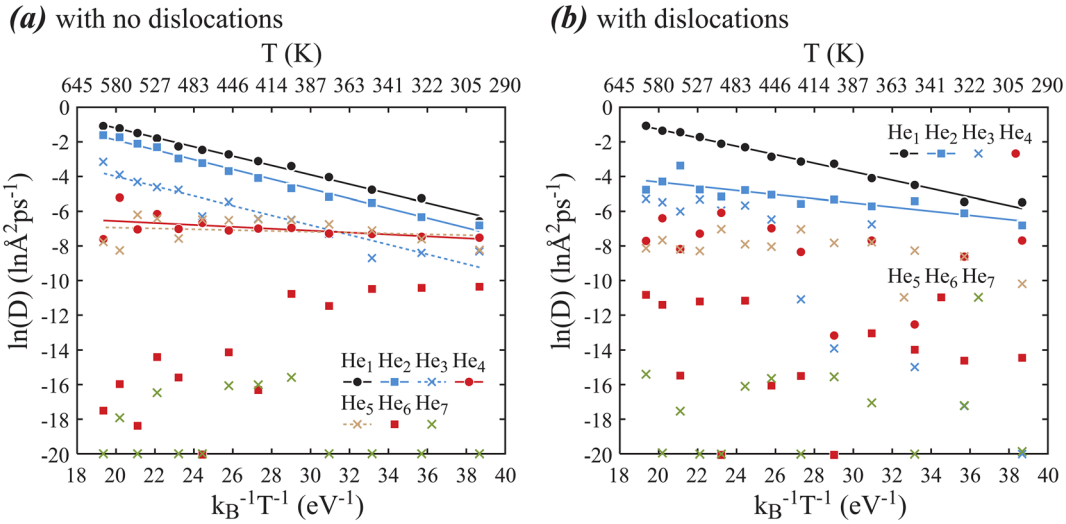

Fig. 3 Logarithm of MD diffusivities for He clusters with sizes 1–7 as a function of $(k_BT)^{-1}$ (k_B is Boltzmann constant and T is temperature): (a) systems with no dislocations, and (b) systems with dislocations.

However, only cluster sizes between 1 and 3 satisfy the Arrhenius equation with clearly defined energy barriers. Diffusivities for cluster sizes 4 and 5 appears independent of temperature and therefore do not represent thermally activated diffusion. In fact, the reduction of diffusivities of cluster sizes 4 and 5 as compared to cluster sizes 1–3 at the high temperature end suggests that cluster sizes 4 and 5 are trapped at certain sites during diffusion. For cluster sizes above 5, $\ln(D)$ is no longer linear with $(k_BT)^{-1}$. In these cases, He clusters are clearly trapped as some of the $\ln(D)$ data points fall at the -20 line. The reason that the other data points do not fall on the $\ln(D) = -20$ line is because it statistically takes various times to reach the trapping sites (*e.g.*, a site with a favorable local composition to form a metal vacancy) and develop the trapping configuration (*e.g.*, a metal vacancy). Considering that the experimental time scales are many orders of magnitude longer than here, clusters with sizes above 5 are likely to always reach trapping sites and therefore exhibit near zero diffusivities in experiments. Hence, we only need to consider diffusivities for cluster sizes 1–5. To provide inputs for mesoscale models to simulate nucleation and growth of He bubbles, the fitted pre-exponential factors and energy barriers are summarized in Table 1 for He cluster sizes 1–5, with the caveat that the parameters for cluster sizes 4 and 5 only reflect MD diffusivities, but may not reflect experimental diffusivities at much longer time scales because they do not satisfy Arrhenius equation as explained above.

Similar analysis is performed for the dislocation cases shown in Fig. 3(b). Here we see that $\ln(D)$ is linear with $(k_BT)^{-1}$ only for cluster sizes 1 and 2, and the larger clusters are more or less trapped as they do not exhibit linear relationships. This is not surprising as not only dislocation core can trap He, but also the dislocation stress field can confine the motion of He clusters. For mesoscale models, we include in Table 1 the fitted pre-exponential factors and energy barriers for He cluster sizes 1 and 2 in the dislocation cases.

The diffusivities discussed above are three-dimensional isotropic diffusivities. Strictly speaking, they are only applicable to dislocation-free systems. When systems contain dislocations, diffusivities parallel and normal to dislocation lines might be different. We use He dimer cluster as an example to explore this. One-dimensional diffusivities along x, y, and z directions are separately calculated based on the previous approach,[43,44] and the results are shown in Fig. 4(a), where for reference the Arrhenius fit to the He_2 diffusivities in dislocation-free system is included as the thick gray line. Fig. 4(a) indicates the dislocations reduce the He_2 diffusivities at high temperatures regardless diffusion directions (x, y, z), suggesting a dislocation trapping effect. Furthermore, Fig. 4(a) shows the

Table 1 Pre-exponential factors D_0 (Å^2 ps^{-1}) and energy barriers Q (eV) for He clusters with sizes 1–5 in systems with and without dislocations (disl)

	He_1		He_2		He_3		He_4		He_5	
Disl	D_0	Q	D_0	Q	D_0	Q	D_0	Q	D_0	Q
No	65.40	0.270	40.090	0.280	4.981	0.28	0.004254	0.055	0.001564	0.024
Yes	35.95	0.244	0.1422	0.119	—	—	—	—	—	—

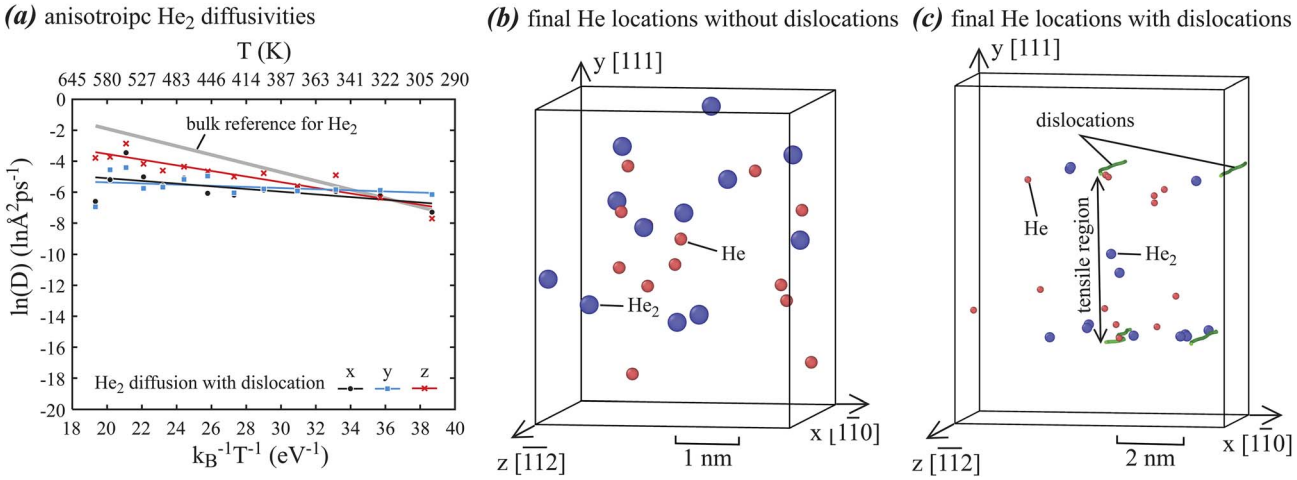

Fig. 4 Results of anisotropic diffusion of He_2 dimer around dislocations: (a) diffusivities, (b) final locations of He and He_2 collected from the 26 diffusion simulations for the dislocation-free systems, and (c) final locations of He and He_2 collected from the 26 diffusion simulations for the dislocation-containing systems.

expected result that diffusion along dislocation line (z) has higher diffusivities than normal to dislocation line (x, and y). On the other hand, diffusivities along x and y are very close. This is interesting because the trapping mechanisms along x and y are different as will be discussed below.

To understand the nature of dislocation trapping, final locations of single He atoms and dimer He_2 clusters obtained from simulations at the 13 temperatures are collectively shown in Fig. 4(b) for systems without dislocations and Fig. 4(c) for systems with dislocations, where small red spheres represent single He atoms and large blue spheres represent He_2 clusters. Fig. 4(b) indicates that the He clusters are more or less uniformly distributed in the dislocation-free systems. In contrast, Fig. 4(c) clearly shows that He clusters are not uniformly distributed in the dislocation-containing systems. In fact, all He clusters are seen in the tensile region between the upper and lower dislocations. Some He clusters are at the dislocation cores. Hence, we see mainly two trapping mechanisms: He clusters are broadly confined within the tensile region of dislocation stress fields, which mainly occur in the y direction in Fig. 4(c), and He clusters can also be trapped at the dislocation cores, which can occur in both x and y directions.

3.2 He-to-bubble time statistics

Four sets of 1000 MD simulations are performed to study the time distribution for a diffusing He atom to join an existing bubble using the method described above. These four sets are respectively applied to systems with no defects, 0.2% vacancies, 0.2% interstitials, and a dislocation dipole. Results of probability for the diffusion He atom not in the bubble are plotted as

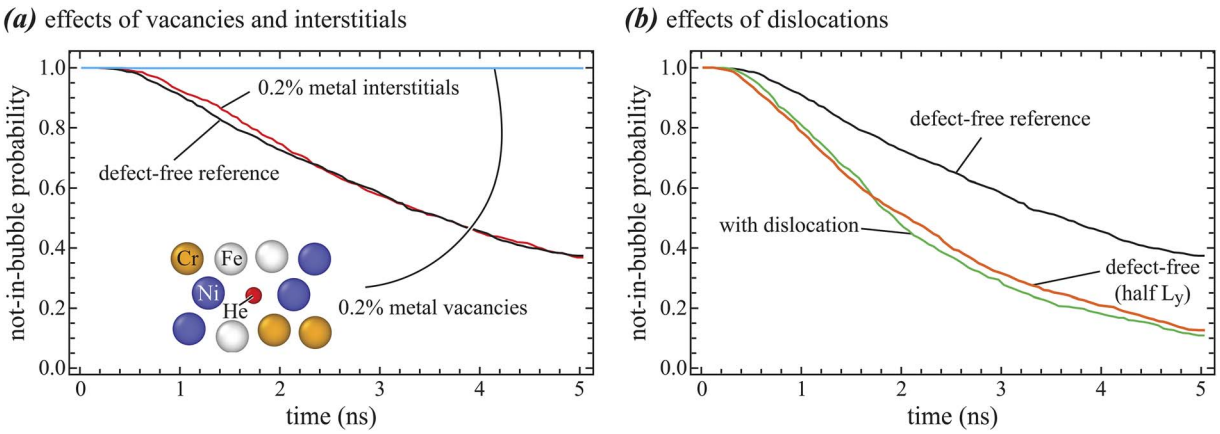

bubble diameter 3.1 nm, initial He atom-bubble spacing 10.6 nm, temperature 800 K, $Fe_{70}Ni_{11}Cr_{19}$

Fig. 5 Time distribution for the diffusion He atom not to join the bubble as a function of time: (a) effects of vacancies and interstitials, and (b) effects of dislocations.

a function of time in Fig. 5, where Fig. 5(a) shows effects of vacancies and interstitials, and Fig. 5(b) shows effects of dislocations.

Fig. 5 shows smooth monotonically decreasing probability distribution curves, verifying that 1000 MD simulations are sufficient to yield reliable results. From Fig. 5(a), we see that the probability distribution curves from systems with no defects and with 0.2% interstitials are very close. Considering that 1000 MD simulations are involved to account for statistics, this strongly indicates that interstitial atoms do not impact the growth of He bubbles.

Interestingly, Fig. 5(a) shows that the probability for the diffusing He atom not to be in the bubble remains to be close to 1 during the entire simulated time of 5 ns when there is 0.2% vacancies. This is dramatically different from the defect-free cases, suggesting that the diffusion He atom is trapped by a vacancy before reaching the bubble. We examine the final locations of the diffusing He atom in 10 of the 1000 simulations, and one example is included in the inlet in Fig. 5(a). In all these 10 cases, a metal atom is missing at the location of the He atom as seen in the inlet. This verifies that the He is trapped by a vacancy. Once trapped by a vacancy, the He cannot no longer reach the bubble by increasing the simulation time. The trapped He essentially nucleates a new bubble as explained above. Hence, vacancies can significantly alter the He bubble nucleation and growth mechanisms.

Fig. 5(b) shows similar probability distribution for systems with dislocations. For comparison, probability distribution for the defect-free systems is included. It can be seen that dislocations significantly reduce the time for the diffusing He to join an existing bubble. This is surprising because dislocations were thought to increase the join time as they can trap the diffusing He just like vacancies. From Fig. 4(c), we see that the main role of dislocations is to confine the motion of the He atom within a tensile region of dislocations. Our existing bubble also lies in this region. This is the likely scenario in experiments because bubbles are more likely to form in regions with high He concentrations which are essentially the tensile regions of dislocations. In addition, He is decayed from ^{3}H and ^{3}H concentration is also elevated in the tensile regions of dislocations due to the formation of a Cottrell atmosphere.[25] Because the diffusion He atom is confined within a smaller volume around the bubble, it is not surprising that the time to join the bubble is reduced.

To verify that the reduction in join time due to dislocations is indeed caused by reduced volume, we perform another set of 1000 MD simulations without dislocations, but with system dimension in y reduced by half so that system volume exactly equals to the volume of the tensile region shown in Fig. 2(b). The probability distribution from these simulations is included in Fig. 5(b). Remarkably, the distribution curve of reduced dimension is in excellent agreement with the one with dislocations. This strongly confirms that the tensile regions of dislocations can promote the growth of bubbles within the same regions.

It should be noted that the dislocations simulated here are ideally straight and are dissociated into partials. In real samples, dislocations are more likely to form a network where perfect dislocation nodes exist. This perfect dislocation nodes are likely to trap He atoms just like vacancies. In that case, dislocations can increase the join time to existing bubbles and promote nucleation of new bubbles.

4. Conclusions

Systematic molecular dynamics simulations have been performed to understand helium bubble nucleation and growth mechanisms in $Fe_{70}Ni_{11}Cr_{19}$ stainless steels. We find that not only single helium atoms, but also small helium clusters, can diffuse in the alloys. The diffusion of these clusters can be significantly reduced by defects such as vacancies and dislocations due to the defect trapping effects. Because the trapping is local, vacancies significantly increase the time for helium atoms to join existing bubbles. As a result, vacancies promote the nucleation of new bubbles as opposed to the growth of existing bubbles. Interestingly, dislocations create a broad tensile region to confine the diffusing helium. This can result in a reducing in the time for helium to join existing bubbles within the same region. Hence, dislocations promote bubble growth in their tensile regions.

5. Appendix

Scales of MD simulations are briefly summarized in Table 2.

Table 2 Summary of MD simulations: number of simulations per set N_{sim}, number of atoms in each simulation N_{atom}, temperature T (K), equilibration time t_{eq} (ns), and production time t_{pro} (ns)

N_{sim}	N_{atom}	T	t_{eq}	t_{pro}	N_{sim}	N_{atom}	T	t_{eq}	t_{pro}
Cluster diffusivities in bulk					Cluster diffusivities with dislocations				
130	7681–7690	300–600	0.2	70	130	30 241–30 250	300–600	0.2	70
He-to-bubble in bulk					He-to-bubble with dislocations				
1000	179 977	800	0.1	5	1000	178 248	800	0.1	5
He-to-bubble with vacancies					He-to-bubble with interstitials				
1000	179 620	800	0.1	5	1000	180 334	800	0.1	5
He-to-bubble in bulk with half dimension									
1000	89 977	800	0.1	5					

Author contributions

Xiaowang Zhou: conceptualization, data curation, formal analysis, funding acquisition, investigation, methodology, project administration, writing – original draft, writing – review and editing.

Conflicts of interest

There are no conflicts of interest to declare.

Acknowledgements

Sandia National Laboratories is a multi-mission laboratory managed and operated by National Technology and Engineering Solutions of Sandia, LLC, a wholly owned subsidiary of Honeywell International, Inc., for the U.S. Department of Energy's National Nuclear Security Administration under contract DE-NA-0003525. The views expressed in the article do not necessarily represent the views of the U.S. Department of Energy or the United States Government.

References

1 H. Ullmaier, Introductory remarks: helium in metals, *Rad. Effects*, 1983, **78**, 1.
2 H. Ullmaier, The influence of helium on the bulk properties of fusion reactor structural materials, *Nucl. Fusion*, 1984, **24**, 1039.
3 S. L. Robinson and G. J. Thomas, Accelerated fracture due to tritium and helium in 21-6-9 stainless steel, *Metall. Trans. A*, 1991, **22**, 879.
4 Y. Dai, J. Henry, Z. Tong, X. Averty, J. Malaplate and B. Long, Neutron/proton irradiation and He effects on the microstructure and mechanical properties of ferritic/martensitic steels T91 and EM10, *J. Nucl. Mater.*, 2011, **415**, 306.
5 N. Yamamoto, T. Chuto, Y. Murase and J. Nagakawa, Correlation between embrittlement and bubble microstructure in helium-implanted materials, *J. Nucl. Mater.*, 2004, **329–333**, 993.
6 S. S. Vagarali and G. R. Odette, A creep fracture model for irradiated and helium injected austenitic stainless steels, *J. Nucl. Mater.*, 1981, **103–104**, 1239.
7 D. Kramer, H. R. Brager, C. G. Rhodes and A. G. Pard, Helium embrittlement in type 304 stainless steel, *J. Nucl. Mater.*, 1968, **25**, 121.
8 W. Qin, A. K. Chauhan and J. A. Szpunar, Helium bubble nucleation at grain boundaries and its influence on intergranular fracture, *Philos. Mag.*, 2019, **99**, 679.
9 S. H. Li, J. T. Li and W. Z. Han, Radiation-induced helium bubbles in metals, *Materials*, 2019, **12**, 1036.
10 J. Henry, L. Vincent, X. Averty, B. Marini and P. Jung, Effect of a high helium content on the flow and fracture properties of a 9Cr martensitic steel, *J. Nucl. Mater.*, 2007, **367–370**, 411.
11 T. Miura, K. Fujii and K. Fukuya, Micro-mechanical investigation for effects of helium on grain boundary fracture of austenitic stainless steel, *J. Nucl. Mater.*, 2015, **457**, 279.
12 D. K. Matlock and W. D. Nix, Effects of helium on the high-temperature creep and fracture properties of Ni-6%W, *J. Nucl. Mater.*, 1975, **56**, 145.
13 C. D. Judge, N. Gauquelin, L. Walters, M. Wright, J. I. Cole, J. Madden, G. A. Botton and M. Griffiths, Intergranular fracture in irradiated Inconel X-750 containing very high concentrations of helium and hydrogen, *J. Nucl. Mater.*, 2015, **457**, 165.
14 H. Schroeder and D. N. Braski, The effect of implanted helium on the high temperature mechanical properties of a model austenitic Fe-17%Cr-17%Ni alloy, *J. Nucl. Mater.*, 1983, **115**, 297.
15 A. A. Sagues, H. Schroeder, W. Kesternich and H. Ullmaier, The influence of helium on the high temperature mechanical properties of an austenitic stainless steel, *J. Nucl. Mater.*, 1978, **78**, 289.
16 X. W. Zhou, M. E. Foster and R. B. Sills, Molecular dynamics studies of helium bubble effects on grain boundary fracture vulnerabilities in an $Fe_{70}Ni_{11}Cr_{19}$-1%H austenitic stainless steel, *J. Nucl. Mater.*, 2022, **565**, 153753.
17 M. Li and S. J. Zinkle, Fracture mechanism maps in unirradiated and irradiated metals and alloys, *J. Nucl. Mater.*, 2007, **361**, 192.
18 F. Roters, P. Eisenlohr, L. Hantcherli, D. D. Tjahjanto, T. R. Bieler and D. Raabe, Overview of constitutive laws, kinematics, homogenization and multiscale methods in crystal plasticity finite-element modeling: theory, experiments, applications, *Acta Mater.*, 2010, **58**, 1152.
19 J. Shi, X. Liu, L. Peng, J. Huang, H. Sun and J. Li, Atomic-scale mechanisms of He/V ratio effect on helium bubble hardening in iron for neutron irradiated F/M steels, *J. Nucl. Mater.*, 2020, **542**, 152495.
20 W. R. Jian, M. Zhang, S. Xu and I. J. Beyerlein, Atomistic simulations of dynamics of an edge dislocation and its interaction with a void in copper: a comparative study, *Modelling Simul. Mater. Sci. Eng.*, 2020, **28**, 045004.
21 Y. N. Osetsky and R. E. Stoller, Atomic-scale mechanisms of helium bubble hardening in iron, *J. Nucl. Mater.*, 2015, **465**, 448.
22 S. M. H. Haghighat and R. Schaublin, Influence of the stress field due to pressurized nanometric He bubbles on the mobility of an edge dislocation in iron, *Philos. Mag.*, 2010, **90**, 1075.
23 S. M. H. Haghighat, G. Lucas and R. Schaublin, Atomistic simulations of He bubble in Fe as obstacle to dislocation, *IOP Conf. Ser. Mater. Sci. Eng.*, 2009, **3**, 012013.
24 M. J. Demkowicz, A threshold density of helium bubbles induces a ductile-to-brittle transition at a grain boundary in nickel, *J. Nucl. Mater.*, 2020, **533**, 152118.
25 G. M. de Bellefon and J. C. van Duysen, Tailoring plasticity of austenitic stainless steels for nuclear applications: review of mechanisms controlling plasticity of austenitic steels below 400°C, *J. Nucl. Mater.*, 2016, **475**, 168.
26 C. Sun, S. Zheng, C. C. Wei, Y. Wu, L. Shao, Y. Yang, K. T. Hartwig, S. A. Malay, S. J. Zinkle, T. R. Allen, H. Wang

and X. Zhang, Superior radiation-resistant nanoengineered austenitic 304L stainless steel for applications in extreme radiation environments, *Sci. Rep.*, 2015, **5**, 7801.

27 C. D. Spataru, K. Chu, R. B. Sills and X. W. Zhou, Molecular statics analyses of thermodynamics and kinetics of hydrogen Cottrell atmosphere formation around edge dislocations in aluminum, *JOM*, 2020, **72**, 3021.

28 X. W. Zhou, M. E. Foster and R. B. Sills, Enabling molecular dynamics simulations of helium bubble formation in tritium-containing austenitic stainless steels: an Fe-Ni-Cr-H-He potential, *J. Nucl. Mater.*, 2023, **575**, 154232.

29 G. J. Thomas and J. M. Mintz, Helium bubbles in palladium tritide, *J. Nucl. Mater.*, 1983, **116**, 336.

30 D. F. Cowgill, Helium nano-bubble evolution in aging metal tritides, *Sandia report SAND 2004-1739*, 2004.

31 D. F. Cowgill, Helium nano-bubble evolution in aging metal tritides, *Fusion Sci. Technol.*, 2005, **48**, 539.

32 K. Morishita, R. Sugano and B. D. Wirth, MD and KMC modeling of growth and shrinkage mechanisms of helium-vacancy cluster in Fe, *J. Nucl. Mater.*, 2003, **323**, 243.

33 J. Boisse, A. de Backer, C. Domain and C. S. Becquart, Modeling of the self trapping of helium and the trap mutation in tungsten using DFT and empirical potentials based on DFT, *J. Nucl. Mater.*, 2014, **29**, 2374.

34 X.-C. Li, Y.-N. Liu, Y. Yu, G.-N. Luo, X. Shu and G.-H. Lu, Helium defects interactions and mechanism of helium bubble growth in tungsten: a molecular dynamics simulation, *J. Nucl. Mater.*, 2014, **451**, 356.

35 H. Q. Deng, W. Y. Hu, F. Gao, H. L. Heinisch, S. Y. Hu, Y. L. Li and R. J. Kurtz, Diffusion of small He clusters in bulk and grain boundaries in α-Fe, *J. Nucl. Mater.*, 2013, **442**, S667.

36 D. Terentyev, N. Juslin, K. Nordlund and N. Sandberg, Fast three dimensional migration of He clusters in bcc Fe, and Fe-Cr alloys, *J. Appl. Phys.*, 2009, **105**, 103509.

37 X.-C. Li, W. Shu, P. Tao, Y. Yu, G.-J. Niu, Y. Xu, F. Gao and G.-N. Luo, Molecular dynamics simulation of helium cluster diffusion and bubble formation in bulk tungsten, *J. Nucl. Mater.*, 2014, **455**, 544.

38 Y. L. Zhou, J. Wang, Q. Hou and A. H. Deng, Molecular dynamics simulations of the diffusion and coalescence of helium in tungsten, *J. Nucl. Mater.*, 2014, **446**, 49.

39 J. L. Cao and W. T. Geng, Migration of helium-pair in metals, *J. Nucl. Mater.*, 2016, **478**, 13.

40 A. P. Thompson, H. M. Aktulga, R. Berger, D. S. Bolintineanu, W. M. Brown, P. S. Crozier, P. J. in't Veld, A. Kohlmeyer, S. G. Moore, T. D. Nguyen, R. Shan, M. J. Stevens, J. Tranchida, C. Trott and S. J. Plimpton, LAMMPS - a flexible simulation tool for particle-based materials modeling at the atomic, meso, and continuum scales, *Comput. Phys. Commun.*, 2022, **271**, 108171.

41 LAMMPS download site: ***https://www.lammps.sandia.gov***.

42 S. Plimpton, Fast parallel algorithms for short-range molecular-dynamics, *J. Comput. Phys.*, 1995, **117**, 1.

43 X. W. Zhou, C. Nowak, R. S. Skelton, M. E. Foster, J. A. Ronevich, C. San Marchi and R. B. Sills, An Fe-Ni-Cr-H interatomic potential and predictions of hydrogen-affected stacking fault energies in austenitic stainless steels, *Int. J. Hydrog. Energy*, 2022, **47**, 651.

44 X. W. Zhou, R. Dingreville and R. A. Karnesky, Molecular dynamics studies of irradiation effects on hydrogen isotope diffusion through nickel crystals and grain boundaries, *Phys. Chem. Chem. Phys.*, 2018, **20**, 520.

45 M. E. Foster and X. W. Zhou, Molecular dynamics study of grain boundary and radiation effects on tritium population and diffusion in zirconium, *J. Nucl. Mater.*, 2023, **578**, 154376.

46 X. W. Zhou, T. W. Heo, B. C. Wood, V. Stavila, S. Kang and M. D. Allendorf, Temperature- and concentration-dependent hydrogen diffusivity in palladium from statistically-averaged molecular dynamics simulations, *Scripta Mater.*, 2018, **149**, 103.

47 X. W. Zhou, F. El. Gabaly, V. Stavila and M. D. Allendorf, Molecular dynamics simulations of hydrogen diffusion in aluminum, *J. Phys. Chem. C*, 2016, **120**, 7500.

48 X. W. Zhou, R. E. Jones and J. Gruber, Molecular dynamics simulations of substitutional diffusion, *Comput. Mater. Sci.*, 2017, **128**, 331.

49 C. D. Spataru, T. W. Heo, B. C. Wood, V. Stavila, S. Kang, M. D. Allendorf and X. W. Zhou, Statistically averaged molecular dynamics simulations of hydrogen diffusion in magnesium and magnesium hydrides, *Phys. Rev. Mater.*, 2020, **4**, 105401.

50 X. W. Zhou, R. B. Sills, D. K. Ward and R. A. Karnesky, Atomistic calculations of dislocation core energy in aluminium, *Phys. Rev. B*, 2017, **95**, 054112.

51 X. W. Zhou and M. E. Foster, Character angle effects on dissociated dislocation core energy in aluminum, *Phys. Chem. Chem. Phys.*, 2021, **23**, 3290.

52 X. W. Zhou, D. K. Ward, J. A. Zimmerman, J. L. Cruz-Campa, D. Zubia, J. E. Martin and F. van Swol, An atomistically validated continuum model for strain relaxation and misfit dislocation formation, *J. Mech. Phys. Sol.*, 2016, **91**, 265.